Overview of HL-2A Recent Experiments

X.R.Duan[1], Yi Liu[1], M. Xu[1], L.W. Yan[1], Y. Xu[1], X.M. Song[1], J.Q. Dong[1], X.T. Ding[1], L.Y. Chen[1], B. Lu[1], D.Q.Liu[1], J. Rao[1], W.M. Xuan[1], Q.W. Yang[1], G.Y. Zheng[1], X.L. Zou[2], Y. Q. Liu[3], W.L. Zhong[1], K.J. Zhao[1], X.Q. Ji[1], W.C.Mao[1], Q.M.Wang[1], Q. Li[1], J.Y. Cao[1], Z.Cao[1], G.J. Lei[1], J.H. Zhang[1], X.D. Li[1], X.Y. Bai[1], J. Cheng[1], W. Chen[1], Z.Y.Cui[1], L. Delpech[2], P.H. Diamond[4], Y.B.Dong[1], A. Ekedahl[2], T. Hoang[2], Y. Huang[1], K. Ida[5], K. Itoh[5], S.-I. Itoh[6], M. Isobe[5], S. Inagaki[6], D. Mazon[2], S.Morita[5], Y. Peysson[2], Z.B. Shi[1], X.G. Wang[7], G.L. Xiao[1], D.L.Yu[1], L.M.Yu[1], Y.P. Zhang[1], Y. Zhou[1], C.H.Cui[1], B.B.Feng[1], M.Huang[1], Y.G. Li[1], B.Li[1], G.S.Li[1], H.J.Li[1], Qing Li[1], J.F.Peng[1], Y.Q.Wang[1], B.S.Yuan[1], Yong Liu[1] and HL-2A team

[1]Southwestern Institute of Physics, P.O. Box 432, Chengdu 610041, China
[2]CEA, IRFM, F-13108 Saint-Paul-lez-Durance, France
[3]CCFE, Culham Science Centre, Abingdon, Oxfordshire, OX14 3DB, UK
[4]CASS & Department of Physics, UCSD, La Jolla, CA 92093, USA
[5]National Institute for Fusion Science, 322-6 Oroshi-cho, Toki-shi 509-5292, Japan
[6]Research Institute for Applied mechanics, Kyushu University, Kasuga, Kasugakeon 6-1, 816-8580, Japan
[7]Harbin Institute of Technology, Harbin, Hei Long Jiang 150006, China
E-mail contact of main author: duanxr@swip.ac.cn

Abstract. Since the last Fusion Energy Conference, significant progress has been made in the following areas: the first high coupling efficiency of low-hybrid current drive (LHCD) with the Passive-Active Multi-junction (PAM) antenna was successfully demonstrated in H-mode on the HL-2A tokamak.Double critical impurity gradients of electromagnetic turbulence were observed in H-mode plasmas. Various ELM mitigation techniques have been investigated, including supersonic molecular beam injection (SMBI), impurity seeding, resonant magnetic perturbation (RMP) and low-hybrid wave (LHW). The ion internal transport barrier was observed in the neutral beam injection (NBI) heated plasmas. Neoclassical tearing modes (NTMs) driven by the transient perturbation of local electron temperature during the non-local thermal transport events have been observed, and a new-type non-local transport triggered by the ion fishbone was found. Long-lasting runaway electron plateau was achieved after argon injection and the runaway current was successfully suppressed by SMBI. It was found that low-n Alfvenic ion temperature gradient (AITG) modes could be destabilized in Ohmic plasmas even with weak magnetic shear and low pressure gradients. For the first time, the synchronization of geodesic acoustic mode (GAM) and magnetic fluctuations was observed in edge plasmas, revealing the frequency entrainment and phase lock. Spatiotemporal features of zonal flows have also been studied by using multi-channel correlation Doppler reflectometers.

1. Introduction

In recent years the HL-2A tokamak program has been aimed to address the key physic issues relevant to ITER, and to prepare HL-2M and ITER operation as well. In order to achieve the goal, many subsystems such as auxiliary heating and diagnostic systems, have been upgraded or developed. The newly developed 3.7 GHz low-hybrid current drive (LHCD) system in HL-2A consists of a Passive-Active Multi-junction (PAM) launcher [1]. The first LHCD experiments with the PAM in H-mode [2] were carried out. The coupled LHW power reached 900 kW in H-mode plasmas. One H-mode discharge is shown in Fig. 1. The LHW power was successfully coupled at large plasma-launcher gap(e.g. 11cm gap for 0.5MW coupled power), and assisted in triggering and sustaining H-mode. Some advanced diagnostic systems have been developed and upgraded, including a multi-channel HCOOH laser interferometer and polarimeter [3,4] for density and Faraday rotation measurement, a 384-channel electron cyclotron emission imaging (ECEI) system for 2D electron temperature fluctuation measurement[5], a multi-channel correlation Doppler backscattering reflectometer (DBS) for poloidal rotation and turbulence measurement [6], a Doppler coherence imaging system for toroidal rotation measurement, a high-frequency magnetic probe array for detecting high mode-number (m/n=20/30) MHD instabilities [7], a wide-angle infrared (IR) periscopes diagnostic for observing plasma wall interaction in the main chamber, etc. A variety of fuelling techniques, such as massive gas injection (MGI), gas mixture supersonic molecular beam injection (SMBI), have been developed or improved. These upgrades greatly enhanced the capability for the study of advanced plasma physics on the machine.

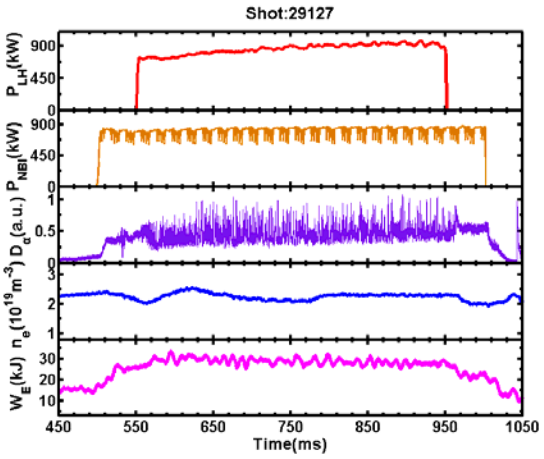

Figure 1. Time evolution of main parameters for the plasmas with coupled LHW power reaching 900 kW in H-mode.

The achieved operation parameters on HL-2A (R = 1.65 m, a = 0.4 m) are as follows. The toroidal magnetic field B_t=2.7 T, plasma current I_p = 430 kA, discharge duration 6.1 s, line-averaged electron density n_e=6×10^{19}m^{-3}， electron and ion temperatures T_e= 5 keV and T_i = 2.8 keV, respectively. The available auxiliary heating and current drive power includes 3MW NBI with two tangential beamlines, 3MW ECRH at 68 GHz and 2MW at 140GHz, and 2MW LHCD at 3.7GHz. Since the last FEC, the experiments on HL-2A have been focused on the investigations on H-mode physics, ELM mitigation and control, core plasma transport, MHD and energetic particle physics, and edge turbulence. In particular the observation of double critical impurity gradients of electromagnetic turbulence [8], role of quasi-coherent mode in pedestal dynamic [9], ELM mitigation and control by SMBI [10], impurity seeding, resonant magnetic perturbation (RMP) and low-hybrid wave (LHW), observation of ion internal transport barrier [11], non-local heat transport induced by fishbone [12], turbulence transition between trapped electron mode and ion temperature gradient mode [13], interplay between neoclassic tearing mode and non-local transport [14], impurity transport [15], mitigation of runaway current with SMBI [16], observation of Alfvenic ion temperature

gradient mode and internal kink mode [17, 19], interaction between magnetic island and geodesic acoustic mode (GAM) [19], and zonal flows measured by Doppler reflectometry [20]. The major experimental results are reviewed in this paper while the details are described in corresponding references.

This paper is arranged as the following. H-mode physics results are given in section 2. ELM mitigation and control by various methods are summarized in section 3. Core plasma transport studies are presented in section 4. MHD and energetic particle physics are discussed in section 5. Edge turbulence studies are shown in section 6. Section 7 is a brief summary.

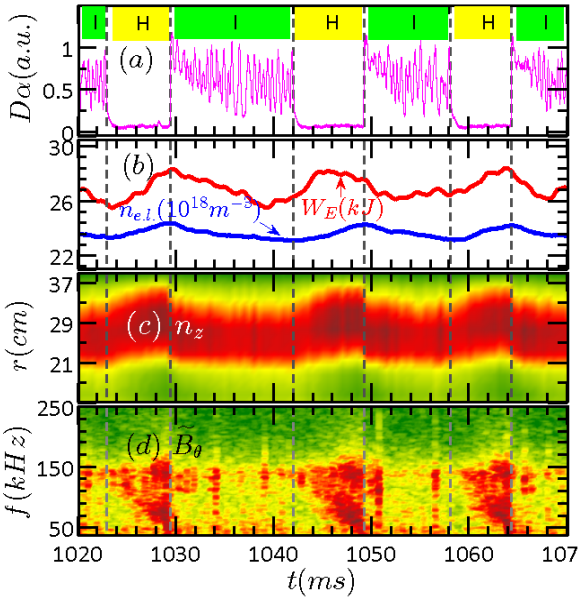

Figure 2. (a) Divertor D_a signal, (b) inner stored energy and line-averaged electron density, (c) effective impurity density, (d) spectrogram of magnetic fluctuations.

2. H-mode physics

In HL-2A, recent experiments in the area of H-mode physics were focused on the study of pedestal dynamics and underlying instabilities. The results presented in this section were from the H-mode discharges with type-III ELMs. The impact of impurity on pedestal dynamics and instabilities has been investigated recently [21]. It was found that a broadband electromagnetic turbulence could be excited by impurities in the H-mode plasmas, and double critical gradients for positive and negative impurity density scale length of the turbulence were observed [8]. In pedestal region, a new pedestal quasi-coherent mode (QCM), which led to an inward particle flux, was observed prior to each ELM onset. It contributes significant additional density and its gradient/pressure gradient increase and may trigger the ELM onset [9].

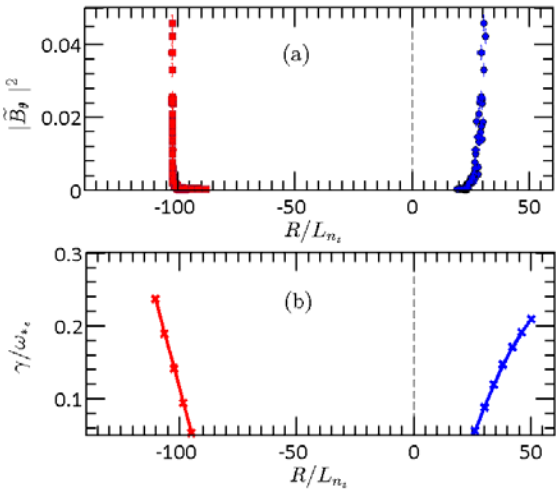

Figure 3. (a) Experimental result: the relation between the intensity of electromagnetic turbulence and the normalized impurity density gradient, (b) simulation results by the HD7 code for electromagnetic turbulence: the normalized linear growth rate of electromagnetic turbulence versus the normalized impurity density gradient.

2.1 Double Impurity Critical Gradients for Electromagnetic Turbulence Excitation

In HL-2A, the impact of impurity on pedestal dynamics and instabilities has been investigated recently. Experimental results have shown that, during the H-mode phase, the impurity was gradually accumulated at the edge plasma region (Fig.2c), where n_z is the effective impurity density deduced from I_{bolm}/n_e,

here I_{bolm} is the emissivity reconstructed

from bolometer array that is mainly contributed by intrinsic impurity and a broadband (frequency of 50-150kHz) electromagnetic turbulence was observed from the spectrogram of magnetic fluctuations (Fig.2d). The excitation of the turbulence was strongly correlated to the accumulation of impurity at the plasma peripheral region. Then the ELM-free phase was ended with the onset of an ELM-like event. After that, the impurity is immediately exhausted, and the plasma transits into the I-phase, with the generation of electrostatic turbulence modulated by limit cycle oscillations. With the gradually increasing pedestal pressure gradient during the I-phase, the plasma returns to the H-mode regime. It suggests that the electromagnetic turbulence plays a key role in the cyclic transitions between the I-phase and H-mode.

Figure 3a illustrates the measured intensity of the electromagnetic turbulence as a function of normalized impurity density gradient in positive and negative gradient regions. Double impurity critical gradients have been observed for the excitation of the turbulence [8]. The critical value of $|R/L_{nz}|$ in positive gradient region is much lower than that in the negative region. The effects of the carbon impurity ions on electromagnetic turbulence have been studied with a gyrokinetic code HD7, which is used to solve the electromagnetic integral eigenmode equations for the study of drift instability [22, 23]. It includes a complete gyrokinetic description for both the main and impurity ion species. The simulation result in Fig.3b also shows double critical gradients in R/L_{nz}. For the turbulence excitation mechanism, the mode is driven by the impurity density gradient in the positive R/L_{nz} region. In the negative R/L_{nz} region, the mode is driven by both impurity and electron density gradients. The results suggest that the observed electromagnetic turbulence could belong to a kind of drift instability which exhibits an electromagnetic feature. The electromagnetic turbulence can also be excited by externally seeded impurity in HL-2A [21]. HL-2A experimental results suggests that the quasi-stationary edge localized impurity profile offers the possibility to actively control the pedestal dynamics and ELMs via pedestal turbulence, which helps to protect plasma facing components.

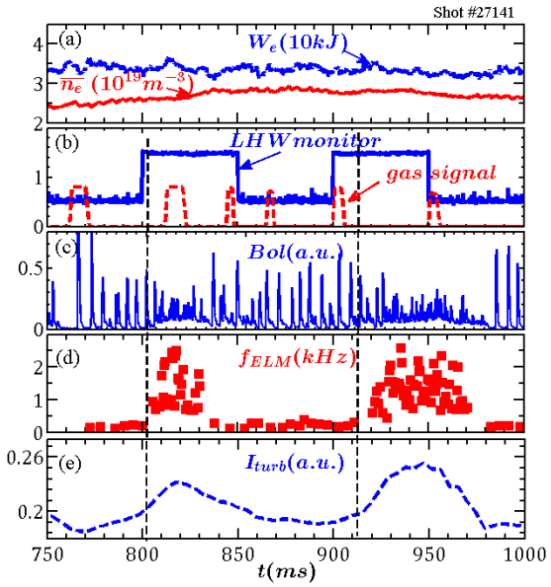

Figure. 4. Time trace of the line-averaged density (red solid line)andthe plasma stored energy（blue dashed line）(a), the LHCD antenna gas puff signal(red dashed line)and the LHW monitoring (blue solid line)(b), the radiation measured by bolometer (c), the ELM frequency (d),and the intensity of the inter-ELM turbulence (e).

3. ELM Mitigation and Control

Various ELM mitigation or control techniques have been explored in HL-2A, including LHW, impurity seeding, RMP, SMBI and pellet injection. ELM mitigation experiments by using new LHW system with the PAM antenna have been performed in HL-2A.The mitigation effect was synchronized with the increase of the pedestal turbulence measured by Doppler

reflectometry. The ELM mitigation has been achieved by externally seeded impurities by means of laser blow-off (LBO) and SMBI systems.With SMBI technique, the experimental results indicated that the shallow deposition (about 20% of pedestal width inside the separatrix) of SMBI is sufficient for ELM mitigation [10, 24]. ELM mitigation by applying n = 1 resonant magnetic perturbation was first obtained in recent HL-2A experiments. It was found that the ELM mitigation window is q_{95} = 3.65-3.85. The drop of core toroidal velocity measured by charge exchange recombination spectroscopy was always observed in ELM mitigation discharges correlated with density pump-out.

3.1 ELM Mitigation with LHCD

Recently LHCD has been shown to be a new method for ELM mitigation [25]. ELM mitigation experiments with LHCD have been performed in HL-2A. Figure 4 shows the typical result. The ELM mitigation is characterized by the increase of the ELM frequency (Fig.4d) and the decrease of the ELM amplitude (Figs.4c and4d). Comparing the LHCD antenna gas puffing signal in Fig.4b with Figs.4c, 4d and 4e, we can conclude that the mitigation effect should not be due to the gas puff from the LHCD antenna, which is designed for improving the coupling of LHW to the plasma when the gap between the plasma and the LHCD antenna mouth is rather large. The image of infrared camera has shown that the divertor heat load released by ELM has been significantly reduced during the mitigation. Generally, the heat flux peak reduces to one third of the original value in average. The mitigation effect with LHCD has also been found to be very sensitive to the parameters as the plasma density and the LHW absorbed power. For high absorbed power, the ELM mitigation effect is more efficient. The desynchronization between LHCD pulse and the ELM mitigation shows that LHCD is only an indirect cause of the mitigation as shown in Figure 4. On the other hand, as shown in Figs.4d and 4e, the mitigation effect is synchronized with the increase of the pedestal turbulence measured by Doppler reflectometry, showing that the enhancement of the particle transport due to the pedestal turbulence could be the direct cause of the ELM mitigation.

3.2ELM Mitigation by Injected Impurity Deposited in Pedestal

In recent HL-2A experiments, the ELM mitigation has been achieved by using different impurities externally seeded by LBO and SMBI systems. Figure 5 illustrates one example which shows the time evolution of the main parameters of one discharge with ELM mitigation. In this discharge, tungsten

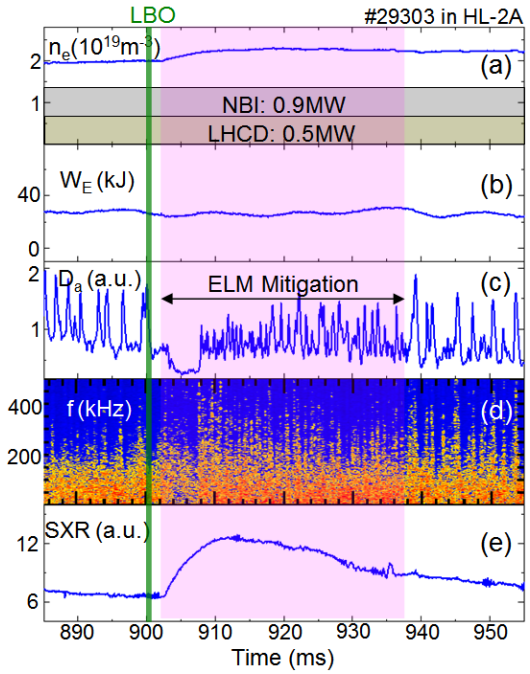

Figure 5. Time evolution of the main parameters of an H-mode discharge with ELM mitigation. (a) Electron density, (b) plasma stored energy, (c) divertor D_a signal, (d) density fluctuation power spectra in pedestal top, (e) soft X-ray emission intensity. The shaded region represents the ELM-mitigation phase.

was seeded by LBO. In addition to ELM mitigation, other purposes of tungsten injection experiment were to study the impurity transport and tungsten spectra. Impurity tungsten was injected into the plasma at t = 900ms. Following the impurity injection, the ELM frequency becomes higher while the amplitude becomes lower, implying that ELMs are mitigated. No obvious degradation of the confinement was observed during the ELM mitigation phase as indicated by the evolution of the plasma stored energy in Fig. 5b. The information of the impurity deposition can be given by the bolometer arrays. The impurity particles can penetrate the edge plasma and were mainly deposited in the pedestal region. The density fluctuations during ELM mitigation phase were significantly increased (as shown in figure 5d), showing that ELM mitigation is strongly correlated to the enhanced transport induced by turbulence in the pedestal. Thus the ELM mitigation may be achieved by the transport enhancement due to the impurity deposition in the pedestal. The induced turbulence by impurity injection might be different from the turbulence triggered by SMBI. Since the impacts of impurity and fuelling on pedestal dynamics are different.

4. Core Plasma Transport

For the progress in core plasma transport, the iITBs were observed in the NBI heated plasmas. The results indicated the importance of flow shear on ITB sustainment [11].The effect of ECRH on the impurity transport has been investigated. The reduction of impurity concentration in the plasmas core was observed when the ECRH power deposited inside the sawtooth reversion surface [15]. A quasi-coherent TEM in spectra of density fluctuations has been observed by multi-channel microwave reflectometers. The turbulence transition and the direct effect of the TEM on particle transport have been studied [13]. For non-local heat transport, it was found that the critical values of β to induce the NTMs in nonlocal discharges were substantially lower than those without nonlocal transport [14].A new-type nonlocal transport triggered by the ion fishbone was observed [12]. These findings revealed the dynamic interaction between turbulence and large-scale mode structures.

4.1 Ion Internal Transport Barriers

The ion internal transport barriers (iITBs) [26, 27] were observed in the NBI heated plasmas on HL-2A [11]. The position of the barrier foot, in the stationary state, coincides with the q=1 flux surface within its uncertainty of measurement. The ion temperature and toroidal rotation profiles are shown in figure 6. For these shots with ITB, long lasting modes (fishbone oscillations [28]) were observed during the peaked ion temperature and velocity phases. Another interesting observation is that the $T_i(\rho=0.5)$ in the discharges without iITBs seems not lower than that with iITBs; and it is clear that the $T_i(0.5)$ declines when the maximum R/L_{Ti} is higher than 14. Further analysis indicates that the $R/L_{Ti}(0.2)$ increases with $R/L_{Ti}(0.5)$ for the discharges without iITB. *W*hen the $R/L_{Ti}(0.2)$ is higher than 14, the iITB is formed. The characters of ion thermal diffusivity indicate that there is a typical ITB in the region ρ<0.4 before ECRH phase. During the ECRH phase without iITB, the

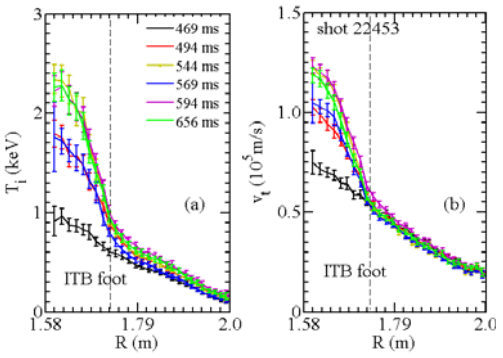

Figure 6. *T_i (a) and v_t (b) profiles.*

χ_i is higher and can be up to ~8 m^2/s. The iITB are observed only in discharges of $T_i \geq T_e$, and are not otherwise, indicating that the temperature ratio plays a very important role in the iITB formation.

The drift turbulence is analyzed with HD7 code and the results indicate that the ITG mode turbulence is dominant for the peaked ion temperature discharges. Providing $E_r \approx v_t B_\theta$, the growth rate of ITG mode is lower than the shearing rate of the flow ($\omega_{E\times B}$) for the whole iITB region, indicating the importance of flow shear on ITB sustainment.

4.2Impurity Transport in ECRH Plasmas

The effect of ECRH on the impurity transport with relation to the ECRH power deposition has been investigated in HL-2A [15], as well as in other devices [29-31]. The reduction of impurity concentration in the plasma core was observed when the ECRH power deposited inside the sawtooth reversion surface. The inversed sawtooth oscillation in the central channels of the soft X ray (SXR) was observed while the normal sawtooth appears at the edge channels of the SXR, as shown in the upper column of figure 7(b).On the other hand, there was no such inversed sawtooth on the central SXR signal with the ECRH power deposited outside the sawtooth inversion surface in the upper column of figure 7(a). Using the SXR measurement the MHD activities with relation to the ECRH (various depositions) are analyzed. Seeing in the lower column of figure 7, a long-lasting m/n=1/1 mode is observed in-between the sawtooth crashes in the inner-deposited ECRH discharge.

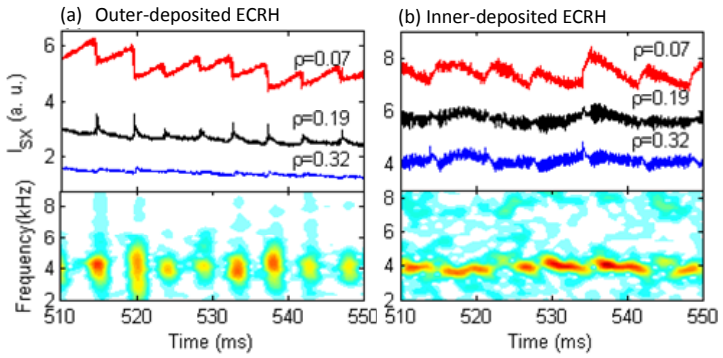

Figure 7. Time revolution of SXR signals for three chords and spectrogram of central SXR chord signal on (a) outer and (b) inner-deposited ECRH discharges.

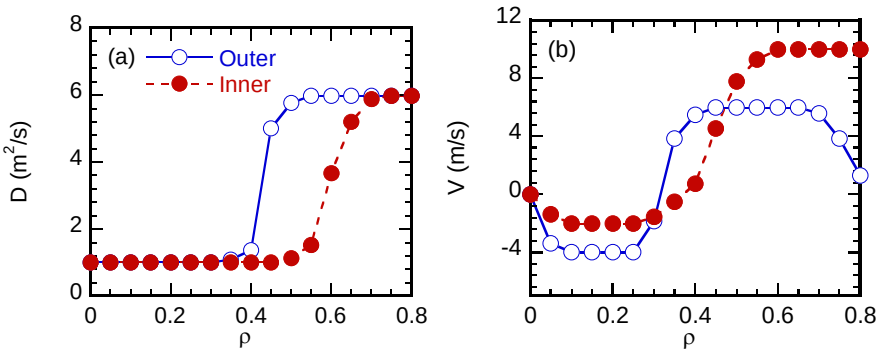

Figure 8. Radial profiles of (a) diffusion coefficient and (b) convective velocity for outer- and inner-deposited ECRH discharges.

Based on the trace impurity injection with the laser blow-off technique, the impurity transport

coefficients were estimated with a one dimensional impurity transport code STRAHL [32]. The results are plotted in figure 8. Both diffusion coefficient D and convection velocity V are increased when the ECRH deposition position shifts inside the sawtooth inversion surface. The V has been greatly reversed to the outward direction with the inner-deposited ECRH but it normally directs inwards in the ohmic discharges. The outward flux of impurity can be significantly enhanced with the inner-deposited ECRH. The calculated Al density profile also confirms that the central peaked impurity density profile has been effectively flattened with the inner-deposited ECRH. During the occurrence of the long-lasting m/n=1/1 mode an outward heat flux has been observed by the ECE measurement.

5. MHD and Energetic Particle Physics

Recently, the behaviors of runaway currents in MGI induced disruptions have been intensively investigated [16]. It was found that the SMBI can suppress the runaway current. The real-time (RT) control of NTMs by ECRH with launcher mirror steering has been developed on HL-2A. The stabilization of tearing modes with the ECRH feedback has been realized. In ohmic plasmas with weak magnetic shear and low pressure gradients, low-n Alfvenic ion temperature gradient (AITG) modes have been observed and identified [17]. Strong resonant and non-resonant internal kink modes were observed [18]. Double m/n=1/1 e-fishbone modes propagating in the opposite directions poloidally were directly observed with the advanced 2D ECEI system in reversed magnetic shear plasma.

5.1 Mitigation of Runaway Current with SMBI

Dedicated experiments have been carried out with the SMBI combined with the MGI on HL-2A [16]. The behaviors of runaway currents in MGI induced disruptions have been investigated. Long-lasting runaway electron (RE) plateau was achieved after argon injection by MGI even at B_t = 1.28 T, much lower than previous B_t threshold found in other tokamaks. It was found that argon injection can cause the generation of runaways carrying up to 30% of the initial plasma current. Moreover, the runaway current caused by

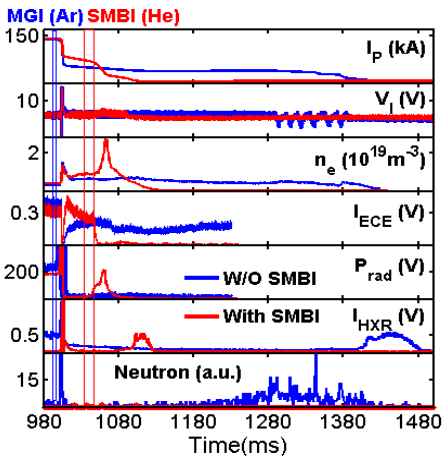

Figure 9 The disruption was triggered by MGI with Ar gas, and then the runaway current was mitigated by using SMBI to inject He gas.

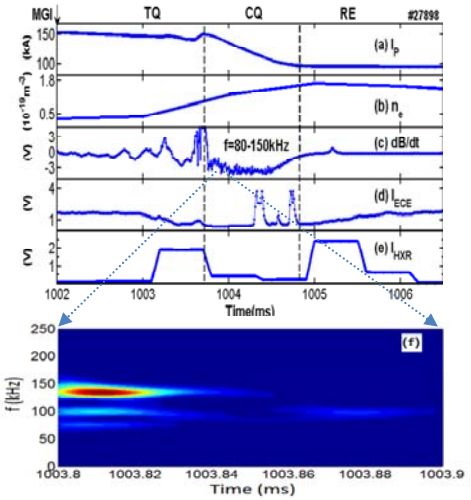

Figure 10. (a) Time traces in the current quench phase showing plasma current I_P, (b) electron density n_e, (c) magnetic instability dB/dt, (d) radiation of Electron Cyclotron Emission I_{ECE}, (e) hard x-ray radiation I_{HXR} and (f) spectrogram of Mirnov signal.

argon injection with MGI was successfully suppressed by SMBI with a number of injected atoms of about 1.0×10^{21}, as shown in figure 9. Light gases, such as helium, are selected in this experiment for its high efficiency in increasing the density. These experiments suggest that SMBI might be viable for runaway suppression in future tokamaks. In addition, a toroidal alfvén eignmode (TAE) -like instability was observed during disruptions deliberately triggered by the MGI of argon, as shown in figure 10. This mode occurs at the beginning of the current quench and lasts about 1-2 ms. These instabilities appears to be favorable in limiting the RE beam formation. It has been found that the runaway plateau is difficult to obtain on the condition of high normalized magnetic fluctuation level($\delta B/B_T$), the runaway plateau is even invisible when $\delta B/B_T$ the exceeds the threshold of about 7.8×10^{-4}, indicating that this magnetic fluctuation plays a scattering role on the RE beam strength.

5.2Real-time Control of Tearing Modes with ECRH

The RT control of NTMs by ECRH with launcher mirror steering has been developed on HL-2A. A few RT diagnostics and intelligent controllers achieved precise control of ECRH deposition at a rational surface. A reliable feedback loop has been designed, developed and tested by a proper integration and coordination of several diagnostic systems with plasma control system (PCS). An RT code solves Grad-Shafranov equation with 129×129 grid scale using the advanced parallel computation within 1 ms. The magnetic island location was determined by the RT 'ECE/Mirnov' subsystem with the high spatial resolution less than 1 cm. Motor controller will calculate the control signal with all the possible signals from the reflective memory networking. The stabilization of tearing modes with the ECRH feedback has been demonstrated on HL-2A, as shown in figure 11. The error bars of the ECRH deposition are the full width at half maximum of the ECRH power deposition area simulated with the code TORAY-GA.

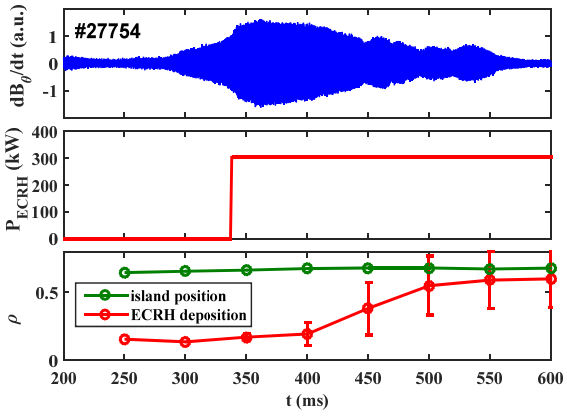

Figure 11. Real time control of tearing mode.

5.3 Low-n AlfvenicIon Temperature Gradient Modes and Internal Kink Modes

Low-n Alfvenic ion temperature gradient (AITG) modes have been observed and identified in HL-2A ohmic plasmas with weak magnetic shear $(s\sim0)$ and low pressure gradients $(\alpha<0.3)$[17]. A group of oscillations with f=15-40 kHz and

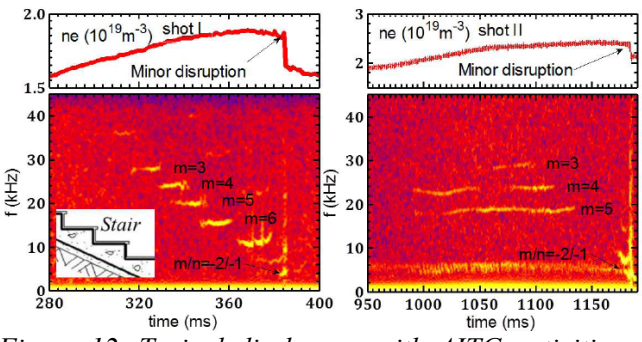

Figure 12. Typical discharges with AITG activities on HL-2A. 2D patterns are spectrograms of ECEI (left) and soft X-ray signal. Left col.(shot I, Bt=1.31T, Ip=150kA) with the frequency staircase; Right col.(shot II, Bt=1.35T, Ip=150kA) with the multi-mode coexistence.

n=3-6 is detected by various diagnostics in high-density ohmic regimes, as figure 12. It was suggested that the modes were excited by pressure gradients. The time trace of the fluctuation spectrogram can be either a frequency staircase, with different modes excited at different times or multiple modes may simultaneously coexist. Theoretical analyses by the extended generalized fishbone-like dispersion relation (GFLDR-E) reveal that the mode frequencies scale with ion diamagnetic drift frequency and η_i, and they lie in KBM-AITG-BAE frequency ranges. AITG modes are most unstable when the magnetic shear is small in low pressure gradient regions. It is worth emphasizing that these instabilities may be linked to the internal transport barrier (ITB) and H-mode pedestal physics for weak magnetic shear.

Strong resonant and non-resonant internal kink modes, abbreviated as RKs and NRKs, were observed [18]. It was found that the RKs and NRKs can be destabilized in reversed q-profile, and the value of q_{min} play an important role in the excitation of the modes. The RK has characteristics of periodic strong bursting amplitude and rapid chirping-down frequency, but the NRK usually has the saturated amplitude, slow changed or constant frequency and long-lasting time, as shown in Fig.13. Frequency of the internal kink modes (IKMs) decreases from about 20 to 5 kHz with plasma current ramping up. These modes poloidally propagate in electron diamagnetic directions.

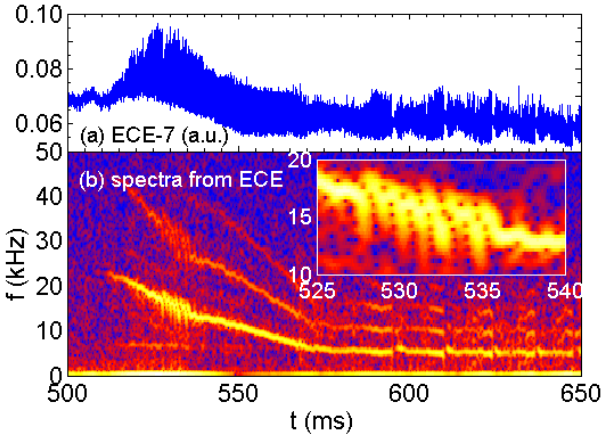

Figure 13. Typical NRK phenomenon on HL-2A. (a) coreECE signal (b) spectrogram of ECE signal.

6. Edge Turbulence

For the first time, the synchronization of geodesic acoustic modes (GAMs) and magnetic fluctuations in the edge plasmas was observed. The frequency entrainment and phase lock were also elucidated [19]. Three-dimensional structures of zonal flows have been studied by using multi-channel correlation Doppler reflectometers. In addition, theoretical predictions of Landau damping and collisional damping for the GAM amplitude were demonstrated [20]. The mechanisms for the generation of blobs/holes at the boundary have been investigated [33].

6.1 Synchronization of GAMs and Magnetic Fluctuations

The interaction between zonal flows and magnetic fluctuations and turbulence was studied in the edge plasmas of the HL-2A tokamak [19]. The frequency entrainment and phase lock, two essential elements, of the synchronization of

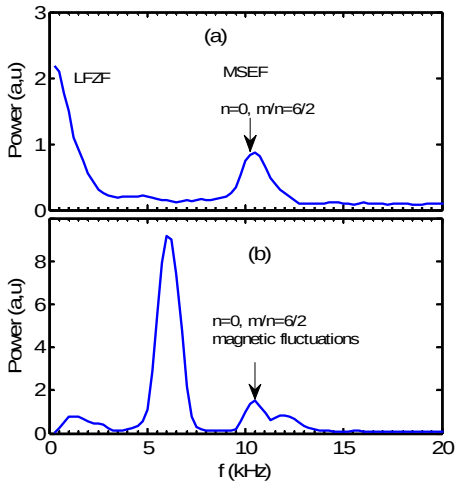

Figure 14 The auto-power spectra of (a) the floating potential fluctuations and (b) the magnetic fluctuations.

GAMs and magnetic fluctuations were measured.

The new meso-scale electric fluctuations (MSEF) with components of the dominant GAMs and the m/n=6/2 potential fluctuations are detected inside the last closed flux surface (LCFS) in ECRH plasmas. The small peak shown in the figure 14(a) at the frequency of ~10.5 kHz is the MSEF. A large power fraction peak of the low frequency zonal flow (LFZF) in the frequency range of ~0.25-3 kHz was also detected. The large peak at the frequency of ~6 kHz shown in figure 14 (b) is the tearing modes with mode numbers of m/n=2/1. The small peak presented in figure 14(b) at the same frequency as the MSEFs has components of the dominant m/n=6/2 magnetic fluctuations and the n=0 zonal field. Besides, the two small peaks at the frequency of 1.2 kHz and 12 kHz come from the power supply and the m/n=4/2 tearing mode, respectively.

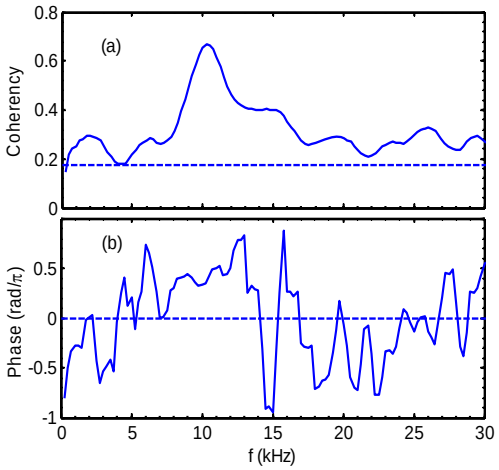

Figure 15. (a) The coherency between floating potential fluctuations and magnetic fluctuations, and (b) their phase shifts.

Figures 15 (a) and (b) show the coherency between floating potential and magnetic fluctuations, and their phase shifts, respectively. The calculated coherency between the MSEFs and the magnetic fluctuations at the MSEF frequency is significantly above the noise level, indicating that the MSEFs are well correlated with the magnetic fluctuations. The phase shift between MSEFs and magnetic fluctuations is ~1.2rad.The temporal evolutions of the MSEFs and magnetic fluctuations and the probability density function (PDF) of the phase shifts between MSEFs and magnetic fluctuations at different time slices were also investigated. This observation results suggest that the frequency entrainment and phase lock between GAMs and magnetic fluctuations exist.

The coupling of the LFZFs and MSEFs to turbulence is an important physics mechanism associated with LFZF and MSEF formation mechanism. Figure 16(a) plots the squared auto-bicoherence of the floating potential fluctuations in the frequency region of f_1<100 kHz, and f_2=-100-+100 kHz. The bicoherence in the frequency region of f_1 = >60 *kHz*, f_2 = ~10.5*kHz*, and $f = f_1 + f_2 \sim 10.5$ *kHz* is significantly above the noise level. This analysis suggests that the turbulence may contribute to the MSEF formation through the nonlinear three

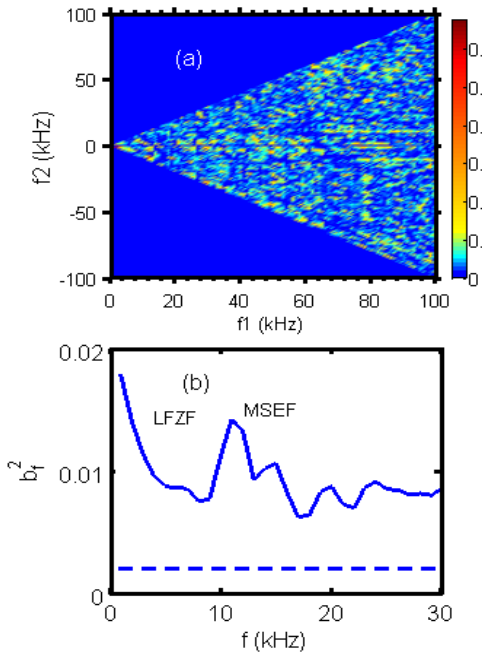

Figure 16. (a) The auto-bicoherence of the floating potential fluctuations, and (b) the summed bicoherence.

wave coupling. In addition, the values of the bicoherences in the frequency region of f_1<=60 *kHz*, f_2 = ~0-4*kHz*, and $f = f_1 + f_2$ ~ 0-4*kHz* are higher. This indicates that the turbulence may also contribute to the LFZF formation. The summed bicoherence is shown in figure 16(b). The peaks in the LFZF and MSEF frequency regions are clearly demonstrated.

The new mechanism for the LFZF formation is the coupling of the MSEFs and LFZFs. This differs from the turbulence driving. Figure 17 gives the zoomed-in plot of figure 16(a). The higher values of the squared auto-bicohence in the frequency region (dashed-ellipses) of f_1 = *9 - 14 kHz*, f_2 =~*0-4kHz*, and $f = f_1 + f_2$ ~ 0-4 *kHz* are apparently shown. The observation suggests that it is possible that the LFZFs are created through three wave coupling between MSEFs and LFZFs.

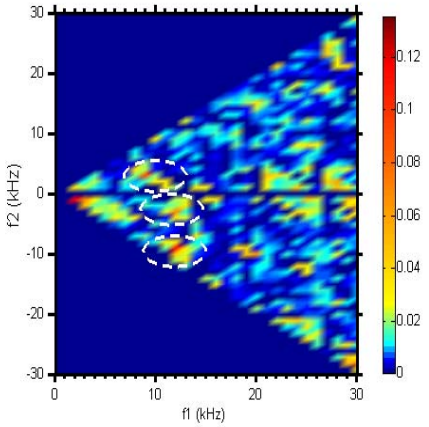

Figure 17. The auto-bicoherence of the floating potential fluctuations.

The characteristic frequency of the observed m/n=6/2 magnetic fluctuations gives us a clue to understand the candidates of the fluctuations. One possibility is a tearing mode because its frequency closes to the plasma toroidal rotation frequency. Another candidate is a BAE due to that its frequency also matches with the GAM frequency. However, further experimental and theoretical works are needed for the identification of the m/n=6/2 magnetic fluctuations.

6.2 Zonal Flows Studied by Multi-channel Correlation Doppler Reflectometry

Recently, the microwave reflectometry, especially the Doppler reflectometry has been developed and improved significantly in HL-2A [6]. Specifically, the oscillations of poloidal plasma flows induced by radially sheared zonal flows were investigated by multi-channel correlation Doppler reflectometers [20]. With poloidally and toroidally equipped Doppler reflectometry, the long range correlation of E_r can be measured. The poloidal and toroidal cross power and phase spectra of E_r fluctuations are shown in figure 18a and 18b. The phase shifts are near zero, demonstrating the two dimensional symmetry (m = 0 and n = 0) of GAM in the electric field fluctuation component. The GAM is believed to be driven by turbulent Reynolds stress by nonlinear three wave interaction. To demonstrate the process, the squared auto-bicoherence of the E_r fluctuations was calculated and shown in figure 18c. The result

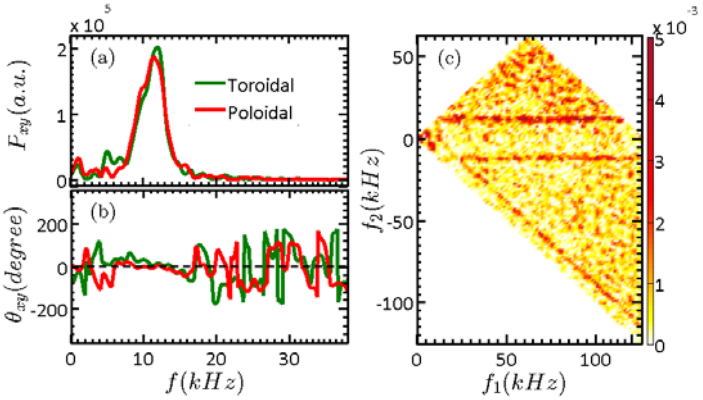

Figure 18. (a) Poloidal and toroidal cross-power spectra of E_r fluctuations between two separated ports and (b) corresponding cross-phase spectra,the distance of two poloidally separated antennas is about 0.3 m. In toroidal direction, the distance is about 1.5 m. (c) Squared bicoherence spectrum of the E_r fluctuation.

indicates that there is nonlinear three wave interaction between GAMs and broadband turbulence, which was demonstrated by nonlinear kinetic energy transfer analysis as the generation mechanism of GAM [34].. Its acoustic property in radial direction was also studied. The coexistence of LFZF and GAM was found. In addition, theoretical predictions of Landau damping and collisional damping for the GAM amplitude were demonstrated.

7. Summary

Experiments on HL-2A produced relevant results for HL-2M and ITER operation and Fusion science. ITER-relevant LHCD launcher has been validated in ITER baseline scenario on HL-2A, and successful coupling of 1MW to L- and H-mode plasmas has been achieved. Double critical impurity gradient of electromagnetic turbulence was observed for the first time in the H-mode plasmas. This result suggests that the quasi-stationary edge localized impurity profile offers the possibility to actively control the pedestal dynamics and ELMs via pedestal turbulence, which helps to protect plasma facing components. ELM mitigation and control has achieved by various techniques, including SMBI, impurity seeding, RMP and LHW, which can reduce the divertor heat load. The ion internal transport barrier was observed in the NBI heated plasmas. The results suggested the importance of flow shear on ITB sustainment. NTMs driven by the transient perturbation of local electron temperature during the non-local thermal transport events have been observed, and a new-type nonlocal transport triggered by the ion fishbone was observed. These findings revealed the dynamic interaction between turbulence and large-scale mode structures. Long-lasting RE plateau was achieved after argon injection by MGI even at B_t = 1.28 T, much lower than previous B_t threshold found in other tokamaks. And the runaway current was successfully suppressed by SMBI. In addition, a TAE-like instability was observed during disruptions deliberately triggered by MGI. It was found that low-n AITG modes (f=15-40 kHz and n=3-6) can be excited in ohmic plasmas with weak magnetic shear and low pressure gradients. Strong resonant and non-resonant internal kink modes were observed in high-power ECRH+ECCD plasmas. For the first time, the synchronization of GAMs and magnetic fluctuations was observed in the edge plasmas. The frequency entrainment and phase lock were also elucidated.. With multi-channel correlation Doppler reflectometers, the symmetric feature of poloidal and toroidal E_r fluctuations of GAM, and its damping mechanisms have been demonstrated.

Acknowledgment

The authors would like to acknowledge all those who have contributed to the HL-2A projects, and are particularly thankful to M. Kikuchi and A. Bécoulet for useful discussion and comments, and the colleagues of IRFM at CEA in France for their dedicated contribution to the HL-2A LHCD system. This work is supported by the Chinese National Natural Science Foundation under grant no 11375053, 11575055 and 11305053, the Chinese National Fusion Projects for ITER under grant no 2013GB104000 and 2014GB108000, and the Chinese International Science and Technology Cooperation Projects under grant no 2015DFA61760.

References

[1] Bai X.Y. *et al.,* Proc. 42nd EPS Conference on Plasma Physics, Lisbon (2015), P5.137. http://ocs.ciemat.es/EPS2015PAP/pdf/P5.137.pdf

[2] Ekedahl, A., *et al.,* 2016 First Experiments in H-mode Plasmas with the Passive-Active Multi junction LHCD Launcher in HL-2A and Impact on Pedestal Instabilities, *Nucl. Fusion* submitted.

[3] Li Y.G. *et al,* 2016 *JINST***11**C02002.

[4] Zhou Y.*et al,*2016 *Rev.Sci. Instrum.***87**,11E,107.

[5] Jiang M. *et.al,* 2015 *Rev. Sci. Instrum*.**83**,10E,336.

[6] Zhong W.L. *et al.,* 2015 *JINST* **10**, P10014.

[7] Xu Yuan *et al.,*2016 *Rev. Sci. Instrum*. **87**, 023507 .

[8] Zhong W.L. *et al.,* 2016 *Phys. Rev. Lett.***117**, 045001.

[9] Dong J.Q. *et al.,* Streamer - A Trigger of Edge Localized Modes, *Nature Communications*, submitted..

[10] Shi Z.B. *et al.,*2016 Role of SMBI deposition in ELM mitigation and the underlying turbulence characteristics, *Nucl. Fusion* sumitted..

[11] Yu D.L. *et al.,* 2016 *Nucl. Fusion* **56** 056003.

[12] Chen W. *et al.,* 2016 *Nucl. Fusion* **56** 044001.

[13] Zhong W.L. *et al. ,*2016 *Phys. Plasmas* **23**, 060702 .

[14] Ji X.Q. *et al.,* 2016 *Sci. Rep.* **6** 32697.

[15] Cui Z.Y.*et al.,* 2016 Study of impurity transport in the HL-2A ECRH L-mode plasmas with radically different ECRH power depositions, *Nucl. Fusion* submitted..

[16] Dong Y.B. *et al.,* Proc. 43rd EPS Conference on Plasma Physics, Leuven (2016), P4.042. http://ocs.ciemat.es/EPS2016PAP/pdf/P4.042.pdf

[17] Chen W. *et al.,*2016 *EPL* **116** 45003.

[18] Yu L.M. *et al.,*2017 *Nucl. Fusion* **57** 036023.

[19] Zhao K.J. *et al.,* 2016 *Phys. Rev. Lett.***117** 145002.

[20] Zhong W.L. *et al.,* 2015 *Nucl. Fusion* **55** 113005.

[21] Zhong W.L. *et al.,* 2017 *Plasma Phys. Control. Fusion* **59** 014030.

[22] Dong J.Q., Chen L., and Zonca F., 1999, *Nucl. Fusion* **39**, 1041.

[23] Lu G.M., et al., 2013, *Phys. Plasmas* **20**, 102505.

[24] Yang Z.C. *et al.,* 2016 *Phys. Plasmas***23** 012515.

[25] Liang Y., *et al*., 2013 *Phys. Rev. Lett* **110**, 235002**.**

[26 Weller A. *et al* 1987 *Phys. Rev. Lett.* **59** 2303.

[27] Kamada Y. *et al* 1991 *Nucl. Fusion* **31** 23.

[28] Chen L., White R.B. and Rosenbluth M.N. 1984 *Phys. Rev. Lett.* 52 1122

[29] R.Neu, et al., Plasma Phys. Control. Fusion 44(2002)811.

[30] J. Hong, et al., Nucl. Fusion 55(2015)063016.

[31] M. Sertoli, et al., Nucl. Fusion 55(2015)113029.

[32] R.Dux, 2006 Technical Report No 10/30 IPP Garching Germany.

[33] Pan O. *et al.,*2016 Investigation of mechanisms for the generation of blobs/holes at the boundary of the HL-2A tokamak, *Nulc. Fusion* submitted.

[34] Xu M. et al., 2012*Phys. Rev. Lett* **108**, 245001.